

Multistable Synaptic Plasticity induces Memory Effects and Cohabitation of Chimera and Bump States in Leaky Integrate-and-Fire Networks

A. Provata · Y. Almirantis · W. Li

Received: October 21, 2024/ Revised version: date

Abstract Chimera states and bump states are collective synchronization phenomena observed independently (at different parameter regions) in networks of coupled nonlinear oscillators. And while chimera states are characterized by coexistence of coherent and incoherent domains, bump states consist of active domains operating on a silent background. Multistable plasticity in the network connections originates from brain dynamics and is based on the idea that neural cells may transmit inhibitory or excitatory signals depending on various factors, such as local connectivity, influence of neighboring cells etc. During the system/network integration, the link weights adapt and, in the case of multistability, they may organize in coexisting excitatory and/or inhibitory domains. Here, we explore the influence of bistable plasticity on collective synchronization states and we numerically demonstrate that the dynamics of the linking may give rise to co-existence of bump-like and chimera-like states simultaneously in the network. In the case of bump and chimera co-existence, confinement effects are developed: the different domains stay localized and do not travel around the network. Memory effects are also reported in the sense that the final spatial arrangement of the coupling strengths reflects some of the local properties of the initial link distribution. For the quantification of the system's spatial and temporal features, the global and local entropy functions are employed as measures of the network organization, while the average firing rates account for the network evolution and dynamics.

A. Provata

Institute of Nanoscience and Nanotechnology, National Center for Scientific Research "Demokritos", 15341 Athens, Greece, E-mail: a.provata@inn.demokritos.gr .

Y. Almirantis

Institute of Nanoscience and Nanotechnology, National Center for Scientific Research "Demokritos", 15341 Athens, Greece, E-mail: yalmir@bio.demokritos.gr .

W. Li

Department of Applied Mathematics and Statistics, Stony Brook University, Stony Brook, NY, USA, and The Robert S. Boas Center for Genomics and Human Genetics, The Feinstein Institutes for Medical Research, Northwell Health, Manhasset, NY, USA, E-mail: wtli2012@gmail.com.

Keywords synchronization; multistable plasticity; synaptic plasticity; weighted network; adaptive network; chimera states; bump states; memory effects; confinement; leaky Integrate-and-Fire model.

1 Introduction

During the past two decades considerable efforts have been devoted to the understanding of complex synchronization phenomena observed in networks of coupled nonlinear oscillators. Such phenomena include traveling waves, spiral (2D) and scroll (3D) waves, chimera states and bump states to name just a few [1, 2, 3, 4, 5]. In particular, the phenomena of hybrid synchronization (chimera states or bump states) were unexpected since they were first shown to occur in networks consisting of identical elements with identical linking between nodes and were, therefore, associated with spatial symmetry breaking in the network [6, 7]. While in the earlier works the connectivity in the system was considered to be constant/uniform or random or statistically homogeneous, in recent years the research interest is shifted toward temporal and adaptive networks whose link weights depend on time and they may gradually develop heterogeneous connectivity properties. Drawing inspiration by the recent advances in the domain of temporal neural networks we here investigate the influence of link adaptivity in the emergence and the form of hybrid synchronization patterns.

From the point of view of applications, the studies of coupled nonlinear oscillators are motivated by brain dynamics, where neural cells operate as potential integrators and they connect with other neural cells via their axons forming large complex networks [8, 9, 10, 11]. The intricate structure of these networks allows the propagation of information in the brain for the control and regulation of a wide variety of body and cognitive functions such as sensory processes, motor actions, thinking, problem-solving, reasoning, learning, memory, emotions, consciousness, homeostasis and many others.

Recent studies of the network structure of the human brain have shown that the connectivity between neural cells is not static but dynamical and changes with time due to aging or diseases or due to the need for adaptation to a constantly changing potential environment [12, 13, 14, 15, 16]. This adaptation process is mainly achieved via plasticity of the connectivity weights. The adaptation of the weights to the local potential environment or to external stimuli is regarded as a learning processes, meaning that the parameters (connectivity weights) in the network are adjusted to optimize the organism's ability to survive, to copy with new challenges, to develop and to respond to life's demands in general.¹ Besides their relevance in life sciences, temporal and adaptive neural networks are now intensively studied in connection with the recent advances in machine learning and artificial intelligence [17]. Motivated by the plasticity of the connectivity weights in brain dynamics, we study here the influence of adaptivity in the formation of hybrid synchronization states, such as chimera states and bump states, using as exemplary dynamics the leaky Integrate-and-Fire (LIF) model.

¹ As will be noted later, in the present work adaptivity and plasticity will be considered with respect to the local weight environment and not to the local potential environment used mainly in the literature.

When studying adaptive connectivity, we keep in mind that there will be an heterogeneity in the coupling weights of the network after adaptation, even if we start from homogeneous or uniformly randomly distributed initial weights. As the original definition of chimera states is based on identical dynamics and identical linking of all nodes [18,19], the patterns resulting due to adaptivity, if composed by co-existing of coherent and incoherent domains in networks with heterogeneous weights, will be called termed “chimera-like” states. Likewise, “bump-like” states will be states composed by coexisting active and subthreshold (silent) domains observed in adaptive networks where the linking between the nodes may not be homogeneous.

Previous studies of complex synchronization phenomena in LIF networks have revealed the presence of chimera states in a 1D ring, 2D toroidal and 3D hypertoroidal geometries under nonlocal connectivity and for relatively large values of the coupling ranges. Studies on 1D ring geometries demonstrate that chimera and multichimera states are possible depending on parameters such as coupling range and coupling strength and on the connectivity schemes (including hierarchical, fractal connectivities) [20, 21, 22, 23, 24, 25]. In 2D toroidal geometries, striking chimera patterns were revealed in the form of coherent or incoherent spots, stripes, grids of spots, spiral waves and other composite patterns [26, 27]. In 3D hypertorus geometries the chimera forms were generalized to coherent and incoherent spheres, cylinders, planes and composite patterns [28]. Concerning the presence of bump states in LIF networks, traveling and spatially confined bumps have been reported in 1D and 2D geometries. The multiplicity of bumps, their size and traveling speed have been shown to depend on the parameter values (coupling strength, coupling range, refractory period, density of inactive nodes etc.) [29, 30, 31, 32, 27, 33, 34].

The chimera and bump states recapitulated in the previous paragraph were all obtained using identical LIF elements on all nodes of the network and identical non-local linking with constant and equal weights. To keep the connectivity geometry identical in all nodes and to avoid boundary value effects all simulations were performed with periodic boundary conditions in one, two or three dimensions. In the present study, we investigate the influence of link adaptivity on the formation of chimera/bump states using as an exemplary case bistable couplings evolving via diffusive non-local interactions [3, 18].

In earlier studies multistability was introduced already in the structural parameters of the single node dynamics. Such attempts include bistability in the internal frequency [35] or in the amplitude [36] of the oscillators. As a result complex frequency and amplitude chimera states were produced as well as frequency-amplitude entanglement effects [36]. In the present study we introduce multistability in the bonding between the different nodes in the network. Synaptic multistability may be induced by the neuron-glia interaction in the brain [37] and its biological meaning is that the strength of the connections between neurons (via the axons) may not be an altogether continuous function but may take specific values, excitatory or inhibitory, leading initially random coupling values to multiple fixed points. As a result, different domains in the system are governed by different coupling parameters and these influence the local firing rates and the internal dynamics. We will demonstrate in the sequel that the effects of introducing bistability in the coupling strength may lead, for specific parameter domains, into coexistence of bumps and chimeras in the same network. Other interesting effects include a) the shift of the coupling parameters where non-trivial composite

chimera-like or bump-like dynamics are observed, b) memory effects in the sense that the final spatial distribution of coupling strengths recalls traces of their initial distribution and c) the presence of a transition point in the coupling range where bistability terminates abruptly giving rise to single fixed point oscillatory dynamics.

We should stress here that the bistable adaptivity rules proposed here are not to be confused with Hebbian like adaptivity, where plasticity depends on the pre- and post-synaptic potentials following the Hebb's principle that "neurons that fire together, wire together" or other spike-timing-dependent plasticity (STDP) models [38, 39, 40, 41]. Rather, in the present study adaptivity/plasticity is inherent in the structure of the neuron axons which are considered to be bistable (or more generally, multistable) and they adapt according to the general tendencies of link weights in the neighboring neural environment [37, 42].

In the next section we present the single/uncoupled LIF model, the ring LIF network and the plasticity rules employed. In Sec. 3 we study the formation of complex chimera-like states under bistability in the link plasticity and in Sec. 4 we examine the influence of link plasticity on the formation of bump-like states. In both Secs. 3 and 4 we provide evidence and stress the presence of spatial memory effects. In Sec. 5 we investigate the effects that link plasticity induces on the network dynamics; namely, we show that multistability on the link weights causes cohabitation of chimera states and bump states on the ring network. In Sec. 6 entropy values are used for the quantification of the network dynamics. Using the local entropy values as quantitative index, we show that for large coupling ranges the system transits from bistable to homogeneous, while the transition R -values depend on the coupling parameters. In the Conclusions section we recapitulate our main results and discuss open problems. To facilitate the reading of this manuscript and to highlight the influence of plasticity in the network, in the two Appendix sections we recapitulate some results on the presence of chimera or bump states in LIF networks without plasticity rules.

2 The model

In this section we present the LIF coupling scheme and its implementation in a 1D ring geometry as will be used in the simulations. The difference of this approach from previous studies in the literature lies in the choice of the coupling terms, which here become time-dependent and adaptive to the neighboring coupling environment.

2.1 The uncoupled LIF dynamics

Historically, the first Integrate-and-Fire neuron models were introduced by Louis Lapicque at the turn of the 20th century to describe the response of nerve fibers to electrical stimuli [43, 44, 45]. The variable $u(t)$ introduced by Lapicque describes the neuron membrane potential which grows linearly due to the interaction with other neurons, up to a threshold potential, u_{th} . After reaching u_{th} the u -variable (membrane potential) is automatically reset to its rest state value, u_{rest} , forming a periodically firing oscillator. A leaky term (proportional to the potential $u_i(t)$) was

introduced to inherently avoid potential divergences in the long time scales and to match experimental observations. The version which includes the leaky term is called ‘‘Leaky Integrate-and-Fire’’ neuron model or simply LIF. The various variations of integrate-and-fire models are very popular amongst computational neuroscientists due to their simple dynamics allowing to consider many thousands up to millions of coupled neurons to mimic realistic natural systems. The choice of the variant depends on the particular application. In the present study the LIF model is employed and the dynamics of the single LIF neural oscillator reads as:

$$\frac{du(t)}{dt} = \mu - u(t) \quad (1a)$$

$$\lim_{\epsilon \rightarrow 0} u(t + \epsilon) \rightarrow u_{\text{rest}}, \quad \text{when } u(t) \geq u_{\text{th}}. \quad (1b)$$

Within the interval $[u_{\text{rest}}, u_{\text{th}}]$ the solution to Eq. (1) can be obtained analytically and the period T_s that the single LIF oscillator takes to fire after rest is calculated as

$$T_s = \ln \left[\frac{\mu - u_{\text{rest}}}{\mu - u_{\text{th}}} \right]. \quad (2)$$

2.2 The coupled and adaptive LIF dynamics

When many LIF elements are coupled on a ring network, the differential equations which describe the evolution of the potential $u_i(t)$ of a neuron at position i on the ring of N neurons are provided below in Eq. (3a) and (3b). Because the coupling strengths are also time dependent, an additional equation, Eq. (3c), is necessary to describe the evolution of the coupling strengths, $\sigma_i(t)$, $i = 1, N$.

$$\frac{du_i(t)}{dt} = \mu - u_i(t) + \frac{1}{2R} \sum_{j=i-R}^{i+R} \sigma_j(t) [u_j(t) - u_i(t)] \quad (3a)$$

$$\lim_{\epsilon \rightarrow 0} u_i(t + \epsilon) \rightarrow u_{\text{rest}}, \quad \text{when } u_i(t) \geq u_{\text{th}}. \quad (3b)$$

$$\frac{d\sigma_i(t)}{dt} = c_\sigma (\sigma_i - \sigma_l)(\sigma_i - \sigma_c)(\sigma_i - \sigma_h) + \frac{s}{2R} \sum_{j=i-R}^{i+R} [\sigma_j(t) - \sigma_i(t)] \quad (3c)$$

In Eqs. (3) the parameter u_{th} is identical for all neurons: when reaching it they reset to their rest potential u_{rest} . μ is the value that the potential of any neuron would asymptotically tend to, if there was no resetting condition; therefore, to achieve periodic firing u_{th} must satisfy the condition $u_{\text{th}} < \mu$. The interaction kernel is assumed to be of rectangular form and every neural oscillator i is linked with all other oscillators j in the range $i - R \leq j \leq i + R$ with adaptive coupling strength $\sigma_i(t)$.

The coupling strengths in Eq. (3c) are assumed to evolve in time following a nonlinear law of order three. The value of the constant c_σ in Eq. (3c) governs the evolution of the coupling strengths. The constants σ_l (standing for σ_{low}), σ_c (standing for σ_{center}), and σ_h (standing for σ_{high}), denote the three fixed points of Eq. (3c) and, without loss of generality, we assume that $\sigma_l < \sigma_c < \sigma_h$. In the same

equation s is a constant related to the connectivity between the coupling of neighboring neurons. In this version of link plasticity each neuron/node i has its own time-dependent coupling strength $\sigma_i(t)$ with the neighbors, while the parameters μ , u_{th} , u_{rest} , R , σ_l , σ_c , σ_h and s are common to all network elements.

As stated in the Introduction, the adaptivity rule introduced in Eq. (3c) is related to the evolution of the various link weights by the influence of their neighboring connectivity. Namely, the evolution of the connectivity σ_i is influenced by the link weights of the neighbors at positions j , where $i - R \leq j \leq i + R$. This adaptivity is not to be confused with Hebbian adaptivity rules, where the evolution of link weights are considered with respect to the potential dynamical variables, u_i and u_j [38,39,40,41].

Biological neurons are known to keep their potential to the rest state for a period of time after firing. This inactive period is called *refractory period* and is denoted by T_r . The refractory period is of the order of T_s , i.e., it accounts for half the period of the single neurons. Earlier studies have shown that hybrid (chimera or bump) states emerge even in the absence of a refractory period [22,46,20,33]. To keep the system as simple as possible, and since the refractory period is not essential for the development of chimera or bump states, a refractory period will not be considered in this study.

In the simulations, aiming to keep the system as generic as possible, we consider random, homogeneous initial conditions both for the initial potentials, $u_i(t=0)$ and coupling strengths, $\sigma_i(t=0)$. The initial states are drawn randomly from uniform distributions such that $0 \leq u_i(t=0) < u_{\text{th}}$ and $-1 \leq \sigma_i(t=0) \leq 1$. The system size needs to be chosen large enough, usually $N \geq 1000$ nodes, to approach asymptotic dynamics avoiding effects related to finite system sizes. To treat all elements equally and avoid boundary effects we use periodic boundary conditions as also discussed in the Introduction. The linear chain containing the N oscillators closes forming a ring and all indices are considered $\text{mod } N$, $u_i(t) = u_{i+N}(t)$ and similarly $\sigma_i(t) = \sigma_{i+N}(t)$. Typical spacetime plots of the network evolution can be viewed in Fig. 1a,b and c for negative fixed points ($\sigma_l, \sigma_c, \sigma_h$) and Fig. 2a,b and c for positive fixed points. Detailed description of these patterns and their properties will follow in Sec. 3 for Fig. 1 and in Sec. 4 for Fig. 2.

2.3 Quantitative measures

To quantify the complexity of synchronization patterns induced by the nonlinearity in dynamics together with the adaptivity of the bondings the most frequently used measure is the average firing rate, or average frequency, f_i , which counts the number of firings of neuron i in the unit of time [18,19]. Namely, if the oscillator i has performed Q_i resettings in the time interval ΔT , the average firing rate is calculated as:

$$f_i = \frac{Q_i}{\Delta T} = \frac{1}{T_i}, \quad i = 1, \dots, N. \quad (4)$$

In Eq. (4), T_i is the period of oscillator i , which may differ substantially from T_s due to the interactions in the network. The average firing rates account for the network evolution and dynamics and they can differentiate between homogeneous and hybrid states only in the case of stable chimeras or bumps. In the case of chimera states, if the coherent and incoherent domains travel in the network,

all network elements spend some amount of time in the coherent motion while for other time intervals they perform incoherent motion. This way, for long time averages all elements acquire a common average firing rate. The same is true for mobile bumps. This is a main disadvantage in the use of the firing rates for distinguishing a traveling chimera state from a purely homogeneous oscillatory network and similarly for traveling bump states.

In the domain of static and dynamical pattern formation the image entropy has been previously employed to identify chimera states in complex coupled maps [47]. Here, the global entropy, $H(t)$, is used to identify the evolution and stability of bumps or chimera states. $H(t)$ is here defined in terms of the homogeneity/heterogeneity of the coupling strengths as:

$$H(t) = - \sum_i^N \tilde{\sigma}_i(t) \log \tilde{\sigma}_i(t) \quad (5a)$$

$$\tilde{\sigma}_i(t) = \frac{|\sigma_i(t)|}{\sum_{j=1}^N |\sigma_j(t)|}. \quad (5b)$$

In case of negative σ_i (inhibitory linking) the absolute values of σ_i are used in Eqs. (5) to calculate $H(t)$ (and later on in Eq. (6) for the calculations of the local entropy). The global entropy, $H(t)$, can not distinguish between moving and immobile chimera and bump states, for the same reasoning as explained above in the case of the average firing rates.

The local entropy evolution, $H_j(t)$, around node j offers information on how the entropy changes locally in time and is calculated as:

$$H_j(t) = - \sum_{k=j-R}^{j+R} \tilde{\sigma}_k(t) \log \tilde{\sigma}_k(t). \quad (6)$$

As in the case of the global entropy, in Eq. (6) for the calculations of the local entropy the absolute values of σ_i are used if σ_i are negative (inhibitory) linking.

Other quantitative measures include the size distribution $P(\sigma)$ of the link weights, the fraction of elements (relative size of) that belong to the active and subthreshold domains [22,33], the distributions of firing rates and link weights. As will be discussed in the next sections the quantitative measures depend on the model parameters, on the connectivity scheme and on the coupling strengths.

Without loss of generality, in the next sections the following working parameter set will be used : $\mu = 1$, $u_{\text{rest}} = 0$, $u_{\text{th}} = 0.98$, $N = 1024$ and $R = 10$ or 40 . The parameters which will be varied for the exploration of the network regimes are σ_l , σ_c , σ_h and R . For the network integration the forward Euler scheme was used with integration step is $dt = 10^{-3}$ TU. Runge-Kutta integration was also employed in some cases for confirmation of the results. The integration mostly takes place for 5000 time units (TU). For the calculation of the firing rates, f_i , $i = 1, \dots, N$, the first 1000 TU are considered as transient and are ignored.

3 The formation of composite chimera-like states due to multistability in the plasticity

As first examples we plot in Figs. 1a, 1b and 1c the spacetime plot of the system, Eqs. (3), starting with three different initial conditions both in the u_i and σ_i variables. All other system and network parameters are the same for all nodes. After the transient states, the three initial conditions drive the system to distinct final states which contain domains with different firing rates and σ -distributions. In particular, in Fig. 1a the system develops one large domain of low firing rates coexisting with a smaller domain of high firing rates. In Figs. 1b and 1c the systems develop two domains of low firing rates coexisting with two domains of high firing rates, the size of the different domains being variable in panels 1b and 1c. The above simulations indicate that the introduction of plasticity in the links introduces a kind of memory effects because the final hybrid states develop domains of different sizes, reflecting the particularities of the initial distribution of the σ_i values. We need to stress here that the fixed points $(\sigma_l, \sigma_c, \sigma_h) = (-0.7, -0.5, -0.3)$ used in the present simulations take all negative values, giving rise to oscillatory dynamics. Because the different σ -values influence locally the system dynamics we observe chimera-like states. Note that in the absence of link-weight evolution (no plasticity, $c_\sigma = s = 0$), the final chimera states of the LIF model develop coherent and incoherent domains whose sizes do not depend on the initial conditions and only the position of the domains may be displaced in the network [22, 23]. For a quick comparison of the LIF network evolution with and without coupling plasticity, we add in the Appendix A typical spacetime plots of the system evolution under different coupling parameters as indicated on the plots.

Regarding the firing rates, for the three different initial conditions shown in Figs. 1a, 1b and 1c the firing rates f_i and the coupling strength σ_i distributions are shown in panels 1d, 1e and 1f, respectively. The spatial distributions of f_i and σ_i also reflect the formation of domains in the system, corroborating the observations in the spacetime plots related to the memory effects, as discussed in Sec. 2.2.

These memory effects are further reflected in the evolution of the global entropy which also depends strongly on the initial conditions. As an example, we plot in Fig. 1g the entropy evolution in the three cases of identical parameters while starting from different initial conditions. We observe that each initial condition (a, b or c) leads to a final state with different entropy. Note that in the case of constant and equal σ_i values, then $\tilde{\sigma}_i = 1/N$. Consequently, a constant value of the entropy is expected only in the case of equipartition and in this case H only depends on the system size as $H = \log N$. For the present system, $N = 1024$ and therefore $H = 6.93$ for constant and equal σ_i , independently of the system parameters. We note that during transient all initial conditions reach H -values close to 6.93 but at the final state they all drop considerably below 6.9, indicating certain degrees of organization.

In panel h of Fig. 1 we plot the local entropy H_i at the final state of the system for the three initial conditions. We may observe that the local entropy drops at the points that correspond to transitions between the different domains. Using Eq. (6) for the case of constant values of σ_i in different local domains of the system, when the domain size is $2R + 1$ the local entropy has the value $H_i = \log(2R + 1)$. For $R = 10$ used in Fig. 1, the local entropy values become $H_i = 3.0445$. Indeed,

such values appear in regions of constant σ_i values, see the corresponding areas in panels 1a, 1b and 1c as well as in 1d, 1e and 1f.

In regions of transition between domains of different σ -values the local entropy drops, as demonstrated by the variations in the H_i in panel 1h. These drops delineate the borders between the different domains of coherence, while the number of entropy maxima or minima can be used to quantitatively count the number of coherent/incoherent domains in the chimera state. The local entropy can be also viewed as an indicator of plasticity and is also linked to the memory of the initial distribution of σ -values.

The results in the present section and in Appendix A are all obtained under negative (inhibitory) coupling strengths. As will be discussed in the next section, Sec. 4, and in Appendix B, in the cases of positive coupling strengths (eg., $(\sigma_l, \sigma_c, \sigma_h) = (0.3, 0.5, 0.7)$ fixed points) bump and bump-like states will be observed.

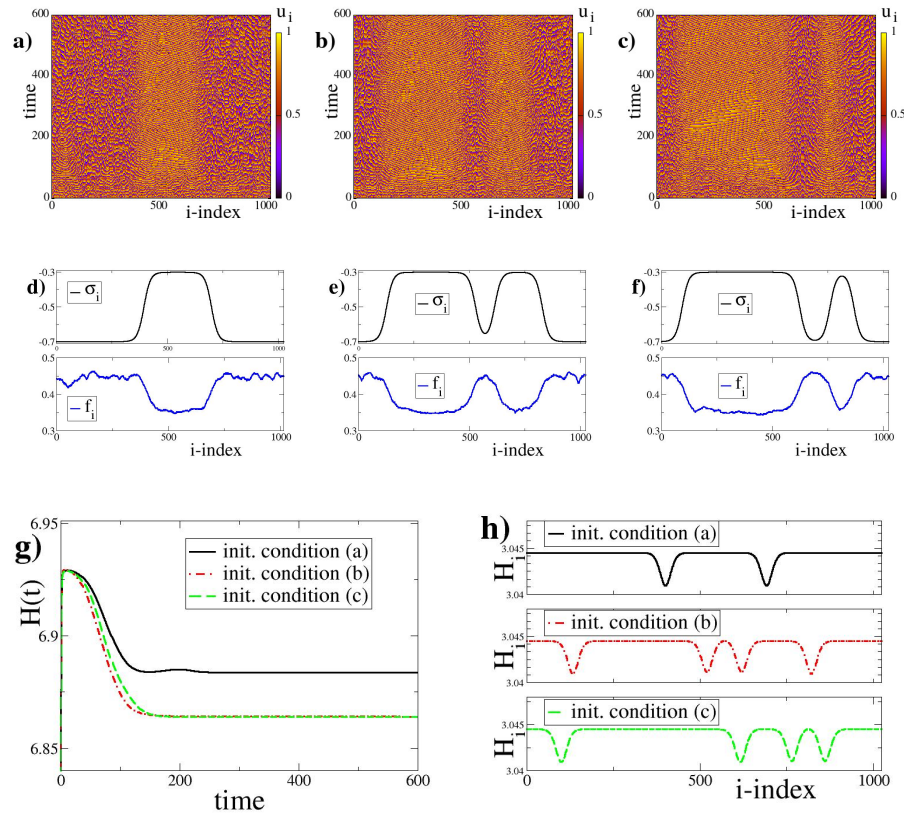


Fig. 1 Coupled LIF dynamics with bistable plasticity and negative coupling strengths. Top row: spacetime plots starting from three different initial conditions are depicted in panels a), b) and c). Middle row : d), e) and f) are the corresponding asymptotic coupling strengths and firing rates for the above three initial conditions. Bottom row: g) The entropy evolution with time, $H(t)$ and h) The local entropy values at the final stages of the simulations. In panels g) and h) the black solid lines correspond to initial condition a), the red dashed-dotted line to b) and the green dashed line to c). The simulations in a), b) and c) start from different random initial conditions in u_i and σ_i . All other parameter values are identical in the three cases: $\mu = 1$, $u_{\text{rest}} = 0$, $u_{\text{th}} = 0.98$, $N = 1024$, $R = 10$, $\sigma_l = -0.7$, $\sigma_c = -0.5$, $\sigma_h = -0.3$, $c_\sigma = -1.0$ and $s = 0.9$.

4 The formation of composite bump-like states due to multistability in the plasticity

In this section we report on the effects of multistable plasticity in the case of positive fixed points σ_h , σ_c and σ_l in the dynamics of the coupling strengths. In parallel to the case of negative (inhibitory) couplings, here we perform numerical integration of Eqs. (3) for positive (excitatory) coupling strengths with $\sigma_l = +0.3$, $\sigma_c = +0.5$ and $\sigma_h = +0.7$, starting with three different random initial conditions in u_i and σ_i . All other parameters are identical to the ones in Fig. 1 following the working parameter set. The results are shown in Fig. 2.

The top row of Fig. 2 presents the spacetime plot of the potentials u_i for three different random initial conditions in u_i and σ_i with all other parameters identical. The time interval is here extended from $t = 0$ to 600 TUs and covers the transient time. In all three cases, Figs. 2a, 2b and 2c, the network nodes spend considerable time near the threshold value (yellow regions) while only occasionally they oscillate and reset to the rest state. This activity is characteristic of bump states, see also Ref. [22] and Appendix B. Because the bump states here (Fig. 2) are formed under adaptivity conditions, where asymptotically the system has reached a state of variable coupling weights, these states will be called “bump-like” states. Moreover, these bump-like states consist of domains where different average firing rates dominate on a silent background of subthreshold elements (yellow regions in Figs. 2a - 2f).

For better inspection of the life and death of the occasional activity in the system, in Figs. 2d, 2e and 2f we present details of the panels 2a, 2b and 2c, respectively. In the 2nd row the time interval is restricted to the last 50 time units, $t = 550 - 600\text{TU}$. The different activity regimes are hard to discern in panels 2a - 2f but they are better visible in the firing rate and coupling strength diagrams. Figure panels 2g, 2h and 2i present the coupling strength and the firing rate spatial distributions starting with the different random initial conditions. We note that in the case of Fig. 2 where coupling strengths are positive the firing rates are considerably lower than in Fig. 1 where the coupling strengths are negative. These lower firing rates are attributed to the tendency of the nodes to stay at subthreshold values for long time intervals and to occasionally perform resettings to the rest state. This has also previously been reported in the case of non-adaptive couplings and for positive coupling strengths, see Ref. [33] and Appendix B.

Memory effects are also evident here. Comparing Figs. 2a, 2b and 2c and corresponding quantitative indices Figs. 2g, 2h and 2i, we understand that the initial (random) spatial distributions of σ_i have given rise to steady states with different domain sizes, influenced by the specific initial $\sigma_i(t = 0)$ states. We recall that in case of identical linking sizes ($\sigma_i = \sigma = \text{const.}$ and without adaptivity) and different initial conditions $u_i(t = 0)$, when chimera states or bump states are formed the distribution of domain sizes remain statistically constant, independent of the randomly chosen initial conditions, $u_i(t = 0)$.

Regarding the entropy evolution in the network, in panel 2j we present the evolution of the global entropy in time for the three different initial conditions. We observe similar approaches to the steady state as in the case of inhibitory dynamics but here the entropy levels attained are different and the first initial condition shows the lowest final entropy (compare with Fig. 1g).

With respect to local entropy, changes in the H_i values occur at the transition regions between active bumps and subthreshold domains, see panel 2k. Similarly to the case of inhibitory coupling, the drops in the local entropy permit to count (quantitative index) the number of active bumps and subthreshold domains of the bump pattern. As in Sec. 3, the local entropy profile also retains some characteristics of the original spatial distribution of the links (memory effects). In addition, adaptivity has caused the shift of bump state formation toward shorter coupling ranges R (in Fig. 2 $R = 10$). This shift in the formation of complex synchronization patterns along with the shifts shown in the case of chimera-like states will be further discussed in Sec. 6.

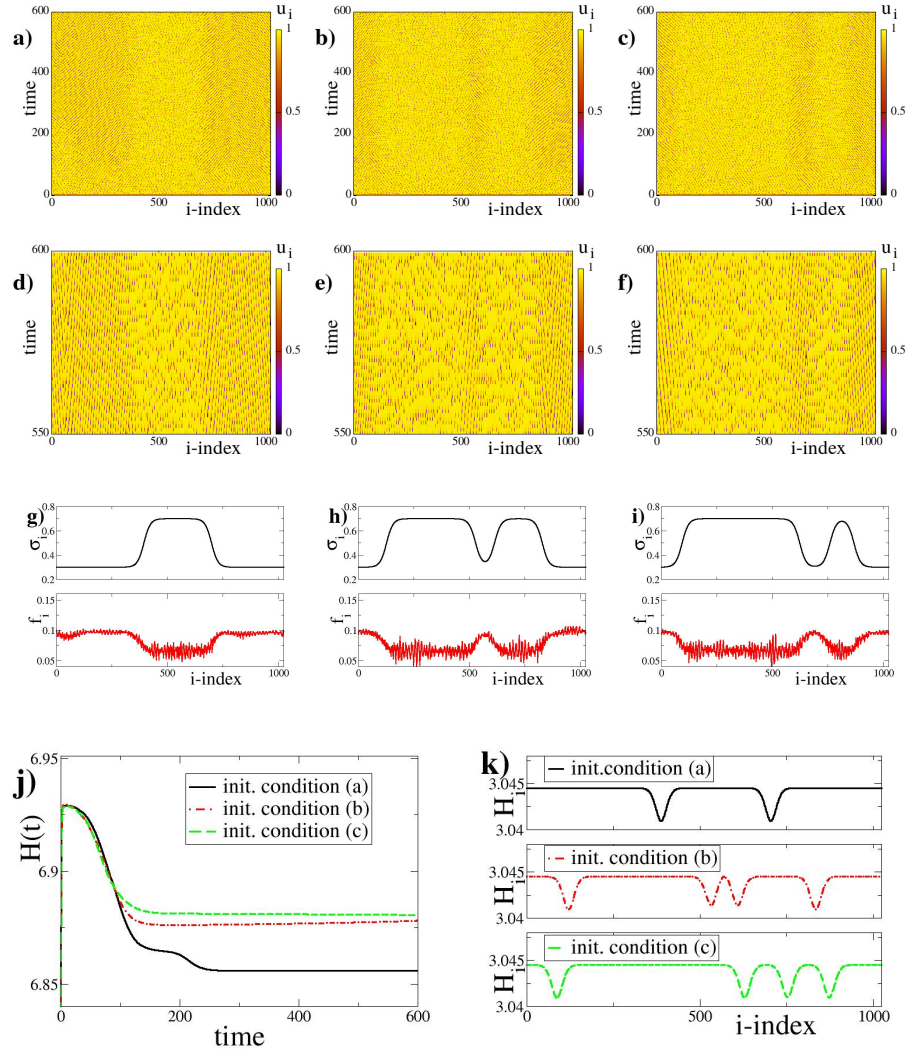


Fig. 2 Coupled LIF dynamics with bistable plasticity and positive coupling strengths. Typical potential spacetime profiles u_i for three different initial conditions a), b) and c) forming bump-like states. For better understanding of the the bump state complexity in the second row panels d), e) and f) show specific details of panels a), b) and c), respectively. Third row : g), h) and i) are the corresponding coupling strengths and firing rates for the above three initial conditions. Forth row: j) The entropy evolution in time, $H(t)$ and k) The local entropy values at the final stages of of the simulations. In panels j) and k) the black solid lines correspond to initial condition a), the red dashed-dotted line to b) and the green dashed line to c). The simulations in a), b) and c) start from different random initial conditions in u_i and σ_i . Coupling fixed point values are: $\sigma_l = +0.3$, $\sigma_c = +0.5$ and $\sigma_h = +0.7$. All other parameter values are the same as in Fig. 1.

5 Coexistence of chimeras and bumps due to multistability in the plasticity

Starting with random coupling strengths distributed on the various nodes of the network (in addition to random initial potentials $u_i(t=0)$), we now concentrate on an exemplary case where the fixed points in the dynamics of the coupling weights (Eq. (3c)) take mixed positive and negative values. Mixed excitatory and inhibitory links are well known to coexist in the same network, notably in the brain dynamical networks [10]. Without loss of generality, we use the working parameter set (see subsection 2.3), with appropriate values of σ_l , σ_c , σ_h and s . The plots in Fig. 3 are representative complex hybrid patterns in the presence of synaptic plasticity with mixed positive and negative fixed points.

More specifically, in Fig. 3 we present typical results of the complex hybrid patterns produced when synaptic plasticity is considered in the coupling strength with $\sigma_l = -0.7$, $\sigma_c = 0.0$, and $\sigma_h = +0.7$. Previous studies have revealed that for negative (inhibitory) coupling strengths chimera states are supported by the LIF network [22, 23], while bumps states appear for positive (excitatory) couplings [33]. By imposing bifurcation conditions in the coupling during the evolution of the LIF network we record hybrid behavior as indicated in Fig. 3a. In this panel we note coexistence of two incoherent domains with domains where subthreshold oscillations persist. Within the subthreshold domains we can record small active bumps. This is further clarified in the spacetime plot of Fig. 3b; here we may first note the presence of yellow subthreshold regions supporting small bumps which move stochastically to the left and right on the ring. The subthreshold regions are separated by active incoherent domains characterized by different u_i values. The positions of the active incoherent and the subthreshold domains on the ring stay fixed in time. In fact, the erratically traveling small bumps in the yellow (subthreshold) regions do not cross the incoherent domains, but they are scattered back by them. In Fig. 3c we record the firing rates and we note that the active domains demonstrate the highest firing frequencies, while the bumps show lower frequencies. The difference in the firing frequencies between bumps and the incoherent domains may be attributed both to the occasional firing and to the motion of the former ones. As the bumps move the energy is transmitted from one element to the neighbors and the firing changes position in time. This means that the elements spend part of their time at the subthreshold state and part in the active state. Because the firing rates are recorded as averages over many time units, they are underestimated in the case of the small mobile bumps. As a result we record lower firing activity inside the subthreshold regions on the positions of the bumps. In Fig. 3d, we plot with black crosses the initial distribution $P(\sigma)(t=0)$ of the coupling strengths σ_i and with red dots the long time (asymptotic) steady state distribution, $P(\sigma)(t=800)$. Because the coupling strengths were initially chosen randomly and homogeneously in the interval $(-1.0, 1.0)$ the initial distribution of σ_i is flat. At the steady state of the network the distribution $P(\sigma)$ becomes bimodal, with maxima at $\sigma \sim \sigma_l = -0.7$ and $\sigma \sim \sigma_h = 0.7$, as formatted by the bistable Eq. 3c.

Another observation worth mentioning is the difference in height in the two maxima of the final bimodal distribution $P(s)$. Indeed, the maximum amplitude corresponding to inhibitory coupling, $P(\sigma \sim -0.7) = 0.12$, is higher than the excitatory coupling one, $P(\sigma \sim +0.7) = 0.04$. This is not unexpected, since the

active chimera-like regions cover a larger number of nodes than the active bumps in the subthreshold regions. Which of the two domains (chimera-like regions or subthreshold regions) will dominate in the final state is, again, a matter of initial conditions.

To the best of our knowledge, complex synchronization patterns composed by bump-like and chimera-like states co-habiting on the network is a direct effect of adaptivity and have not been observed before.

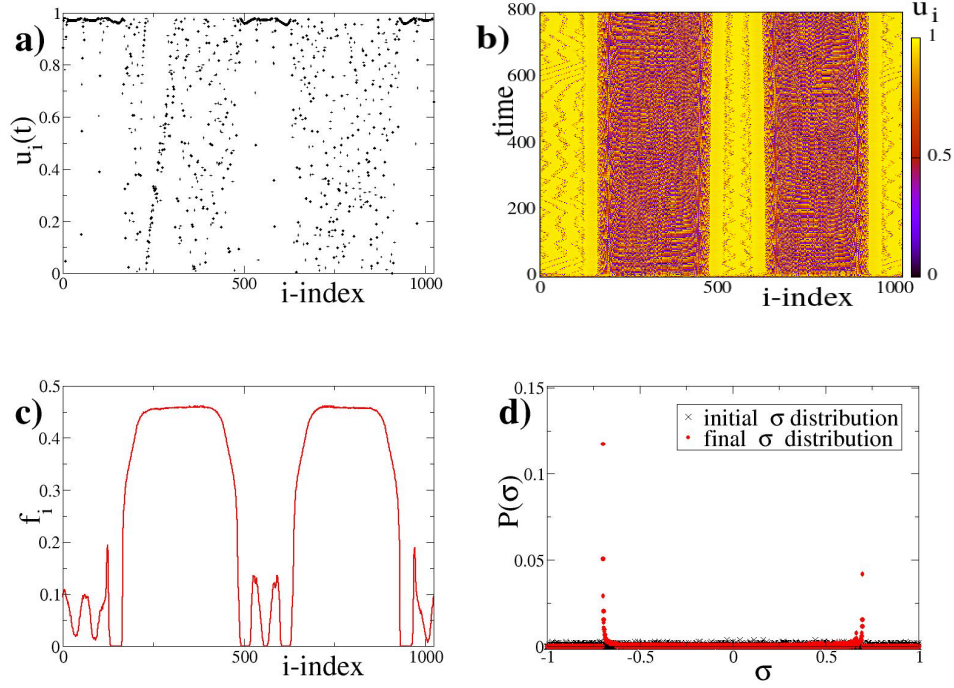


Fig. 3 LIF network with bistable adaptive coupling comprising positive and negative fixed points cause the formation of complex synchronization patterns combining both bump and chimera features. a) Typical snapshot of the neuron potential (time 800 TU), b) spacetime plot c) the average firing rate after 800 TU and d) The distribution of coupling strengths σ at $t = 0$ TU (black crosses, homogeneous random initial conditions) and at $t = 800$ TU (red dots). Parameter values are: $\mu = 1$, $u_{\text{rest}} = 0$, $u_{\text{th}} = 0.98$, $N = 1024$, $R = 40$, $\sigma_l = -0.7$, $\sigma_c = 0.0$, $\sigma_h = +0.7$, $c_\sigma = -1.0$ and $s = 0.9$. Simulations start from random uniform initial conditions in u_i and σ_i .

6 The influence of the coupling range in synaptic bistability

As earlier discussed, one of the effects of synaptic bistability is the presence of chimera or bump states for small values of the coupling range R . We also recall that in these parameter regions ($R \ll$) spatially hybrid states are not formed

for constant or homogeneous linking, see also Appendices A and B. To explore the R -regions where chimera-like or bump-like states are formed due to synaptic bistability we perform numerical simulations of LIF networks for inhibitory and excitatory coupling and R ranging from 1 to 80 lattice units. For quantifying the presence of hybrid states we use the deviation of the local entropy at the asymptotic state, d_H^2 , defined as:

$$d_H^2 = \frac{1}{N} \sum_{j=1}^N [H_{\max} - H_j]^2. \quad (7a)$$

$$H_{\max} = \max\{H_j\}, \quad j = 1 \cdots N. \quad (7b)$$

In Eqs. (7) the values of H_i and H_{\max} are recorded at the asymptotic state, after the transient period.

In Fig. 4 we present variations of d_H with R for inhibitory coupling, using as coupling fixed points the exemplary set $(\sigma_l, \sigma_c, \sigma_h) = (-0.7, -0.5, -0.3)$. The fixed points in the selected set take all negative values leading to inhibitory asymptotic dynamics. Other parameters as in the working parameter set. The solid black line with black circles in Fig. 4 serves as guide for the eyes.

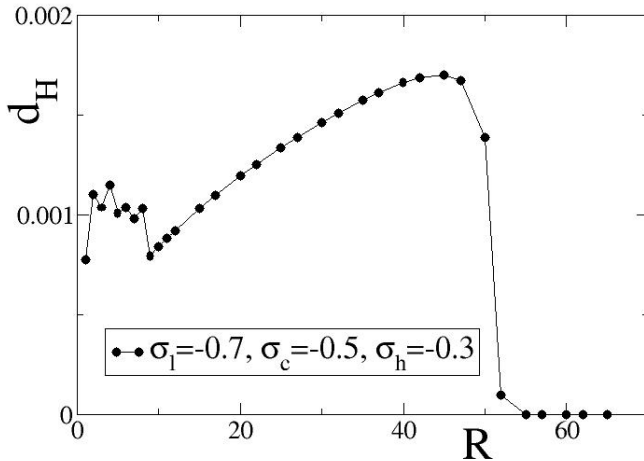


Fig. 4 Local entropy deviations d_H as a function of the coupling range R for inhibitory coupling. Parameter values are: $\sigma_l = -0.7$, $\sigma_c = -0.5$, $\sigma_h = -0.3$. Other parameters are as in Fig. 1. All simulations start from the same random uniform initial conditions both in u_i and in σ_i .

For small values of the coupling range, $R \leq 10$, we observe non-monotonous variations of d_H as a function of R . We note that for $R = 1$ we have the limit of diffusion where hybrid synchronization regimes are not observable. In this short range limit, $1 \leq R \leq 10$, the coupling ranges are very short and any small increase in R may influence substantially the spatial distribution of domains where σ_l or

σ_h dominate. That is the reason of observing the non-monotonous variations in d_H .

For intermediate coupling distances we observe a monotonous increase of d_H with R . As R increases organization takes place in larger and larger domains and this is reflected in the index d_H . For even larger values of R , one of the two stable fixed points prevails and the spatial distribution of link weights becomes homogeneous. As a result all weights become equal and, therefore, $d_H \rightarrow 0$. The shape of d_H vs. R curve in Fig.4 is typical for general inhibitory parameter values but the R -value where the transition from bistability to monostability occurs depends on the precise values of the fixed points $(\sigma_l, \sigma_c, \sigma_h)$. For the exemplary set $(-0.7, -0.5, -0.3)$ the transition occurs at $R \sim 55$, while for $(-0.8, -0.5, -0.1)$ at $R \sim 90$ (not shown). These transition values may also vary slightly for different initial conditions. The difference in the R value where the transition occurs can be dependent also on the length of the interval between the attracting fixed points, which for the case of set $(-0.7, -0.5, -0.3)$ is 0.4, while for set $(-0.8, -0.5, -0.1)$ is 0.7.

In Fig. 5 we examine the case of positive fixed points and present variations of the local entropy deviation d_H with the coupling range R for excitatory coupling. As exemplary set of coupling fixed points we use $(\sigma_l, \sigma_c, \sigma_h) = (+0.2, 0.5, +0.8)$ (the solid red line is set as guide for the eyes). Other parameters as in Fig. 4.

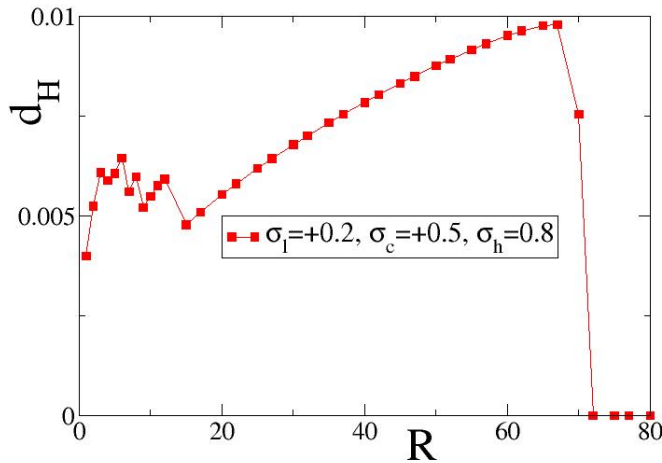


Fig. 5 Local entropy deviations as a function of the coupling range for excitatory coupling. Parameter values are: $\sigma_l = +0.2$, $\sigma_c = +0.5$, $\sigma_h = +0.8$ (red squares-line). Other parameters are as in Fig. 1. All simulations start from the same random uniform initial conditions both in u_i and in σ_i .

As in the case of Fig. 4, in Fig. 5 we also observe non-monotonous variations of d_H vs. R in the small coupling ranges, $1 \leq R \leq 17$. The reason is similar to the case of negative fixed points, namely, for small R -values any increase in R may influence substantially the spatial distribution of domains where σ_l or

σ_h dominate. Similarly, for intermediate coupling ranges we observe a monotonic increase of d_H vs. R up to an R -value where transition occurs and one of the two fixed points, σ_l or σ_h , dominates, leading again to an homogeneous link-weight distribution. For the present parameter values the critical value of R where the transition occurs is 74. Apart from the difference in the transition coupling range, another difference between Figs. 4 and 5 is in the scales of d_H values: the d_H in Fig. 5 are approximately one order of magnitude higher than those in Fig. 4.

Comparing Fig. 4 and Fig. 5, we conclude that the general form of the d_H vs. R curve is essentially conserved for positive or negative adaptive couplings. While the form of the curve is conserved for an extended region of parameter values, the precise R and d_H ranges where the non-monotonous behavior or monotonous increase dominate as well as the R -values where d_H drops to 0 (transition point) depend strongly on the specific coupling parameter values and in particular in the values and the signs of the three fixed points ($\sigma_l, \sigma_c, \sigma_h$).

7 Conclusions

In the present study we concentrate on the influence of bistable plasticity rules in the dynamics of LIF networks. Previous studies have demonstrated the presence of chimera states for inhibitory coupling strengths and bump states for excitatory couplings in nonlocally connected LIF networks. In the case of inhibitory coupling, we show that multistable synaptic rules may shift (lower) considerably the region of coupling ranges where chimera states are observed. Similarly, for the positive couplings, the introduction of bistability in the synaptic strengths lowers considerably the R ranges where bumps occur. In addition, we show that for appropriate choice of the stable synaptic fixed points it is possible to obtain cohabitation of chimera-like and bump-like states simultaneously on the network.

To quantify the presence of chimera/bump states in the network we use the local entropy deviations d_H in the network. Using d_H as an index of synaptic organization, we show that there is a transition point in the coupling range values R where the system transits from multistable to single fixed point dynamics. While the form of d_H vs R retains its qualitative features for large regions of the parameters, the transition R -values depend strongly on the specific coupling parameter values.

Memory effects have also been recorded, where the spatial organization of the final state of the network contains recollection of the original ($t = 0$) distributions of link weights. Therefore, starting from different initial conditions we may end up in final states with statistically different spatial ordering/organization, eventhough all system parameters are kept to the same values.

Direct extensions of this work may include the study of the R -transition as a function of the distance between the stable fixed points σ_l and σ_h or the coupling strength s , as well as various aspects of cohabitation of chimera and bump states simultaneously on the network.

Future extensions may include the possibility of multistable linking $\sigma_{ij}(t)$ which depends both on the pre- and post-synaptic neurons. Other, Hebbian-like plasticity rules [38,39] or spike-timing-dependent plasticity [48] may include nonlinear linking terms depending on the values of the involved potentials u_i and u_j on the last term of the right-hand side in Eq. (3c). In a different direction, yet, we may

consider the influence of a power law distribution on the number of links emanating from the neurons of the network or/and power-law distribution of the link weights. This conforms with recent biomedical studies reporting that the number of synapses per axon follow long-tailed distributions [49] and is in line with Hebb's propositions of long-range distributions in the links per node [38]. This structural property has been recently attributed to the property of preferential attachment of the neurons in the network [50].

8 Acknowledgments

This work was supported by computational time granted from the Greek Research & Technology Network (GRNET) in the National HPC facility - ARIS - under Project ID: PR014004.

Appendices

In the two appendices below we recapitulate some results from earlier publications on the LIF model without adaptation rules. Basically, we integrate Eqs. (3a) and Eq. (3b), while keeping all coupling strengths σ_i to a constant value σ . The constant σ 's are negative in the case of inhibitory coupling (see Appendix Sec. A) and positive in the case of excitatory coupling (see Appendix Sec. B). These results may be found scattered in previous publications, notably in [22, 23, 33]. Here, we provide a short recapitulation of these results for the convenience of the readers and for direct comparison of the LIF networks with and without adaptation rules.

The equations which now describe the system without adaptation are:

$$\frac{du_i(t)}{dt} = \mu - u_i(t) + \frac{\sigma}{2R} \sum_{j=i-R}^{i+R} [u_j(t) - u_i(t)] \quad (\text{A.1a})$$

$$\lim_{\epsilon \rightarrow 0} u_i(t + \epsilon) \rightarrow u_{\text{rest}}, \quad \text{when } u_i(t) \geq u_{\text{th}}. \quad (\text{A.1b})$$

With respect to Eq. (3a), Eqs. (A.1a) has coupling strength σ which is constant in time and takes a value common to all nodes. Eq. (3c) is redundant (not needed) here, since all coupling strengths neither evolve nor adapt in time.

A Results for LIF network without adaptation rule: Inhibitory Coupling

In this section we present the system evolution without coupling plasticity and for negative values of the coupling strength (inhibitory coupling). For comparative reasons we will present spacetime plots for $\sigma = -0.3$ and -0.7 with $R = 10$ and $R = 350$. All other parameters are the same as the ones used in the main text.

In Fig. A.1a we present the spacetime plot of the system for $\sigma = -0.3$ corresponding to the first of the fixed points in the coupling strength (as in Sec. 3 and Fig. 1) and $R = 10$. We see that for homogeneous and short-distance coupling the system, after transient, reaches the homogeneous steady state. For these

couplings strengths ($\sigma = -0.3$) only for long-distance couplings non-trivial effects arise such as coexistence of coherent and incoherent domains, see Fig. A.1b where $\sigma = -0.3$ and $R = 350$. [Nevertheless, careful observations of Fig. A.1a may spot the presence of a single solitary state around $i = 650$, where the node escapes the altogether coherent environment. Solitary states are related to the birth of chimera states.]

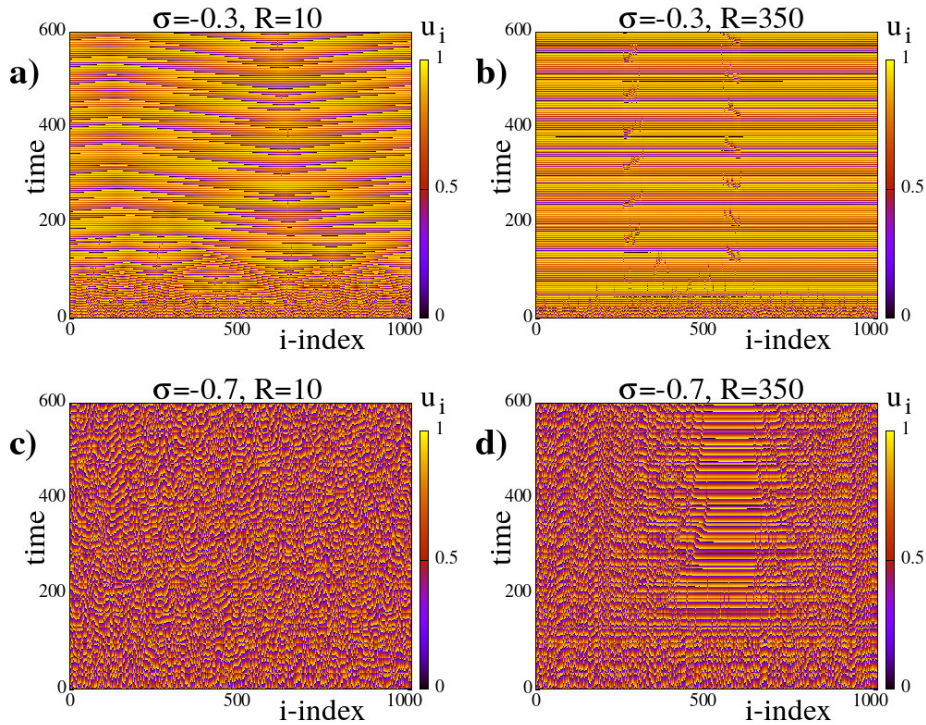


Fig. A.1 Synchronization patterns for inhibitory coupling without link plasticity. Typical spacetime plots for a) $\sigma = -0.3$ and $R = 10$, b) $\sigma = -0.3$ and $R = 350$, c) $\sigma = -0.7$ and $R = 10$, and d) $\sigma = -0.7$ and $R = 350$. All other parameter values are as in Fig. 1 of the main text. Simulations start from the same random initial conditions in $u_i(t = 0)$.

Similarly, in Fig. A.1c we present the spacetime plot of the system for smaller value $\sigma = -0.7$ corresponding to the second attractive fixed point in the coupling strength presented in Sec. 3 and Fig. 1. The coupling range is small, $R = 10$, as in Fig. A.1a and in the other cases of plasticity studied in the main text. We note a certain degree of inhomogeneous firing in the system without indications of coherence. For this coupling strength typical chimera states develop when the coupling range takes large enough values, see Fig. A.1d with $\sigma = -0.7$ and $R = 350$. For a more complete study on the presence of chimera states for negative coupling strengths and different parameter values in the LIF model without plasticity we refer the interested reader to Refs. [22, 23].

B Results for LIF network without adaptation rule: Excitatory Coupling

In analogy with the presentation in the previous appendix section A, we here recall results on the system evolution without coupling plasticity and for positive values of the coupling strength (excitatory coupling).

In this case ($\sigma > 0$ identical for all nodes), the system presents bump states where active elements appear in a background of silent subthreshold elements. Namely, for small values of the coupling range we observe erratically appearing and moving active elements, see the cases of $R = 10$ in Figs. B.1a and B.1c for $\sigma = +0.3$ and $+0.7$, respectively. As R increases, the active nodes organize in domains which travel around the ring with constant velocity. The size of the active traveling domains and their velocity depend on the parameters R and σ , while their direction (left-wise or right-wise) is determined by the initial conditions. Typical examples of traveling bumps are presented in Figs. B.1b and B.1d. These figures indicate that the size of the active traveling bumps increases with σ . Further discussions on studies on bump states in 1D LIF networks without adaptation are presented in Ref. [33].

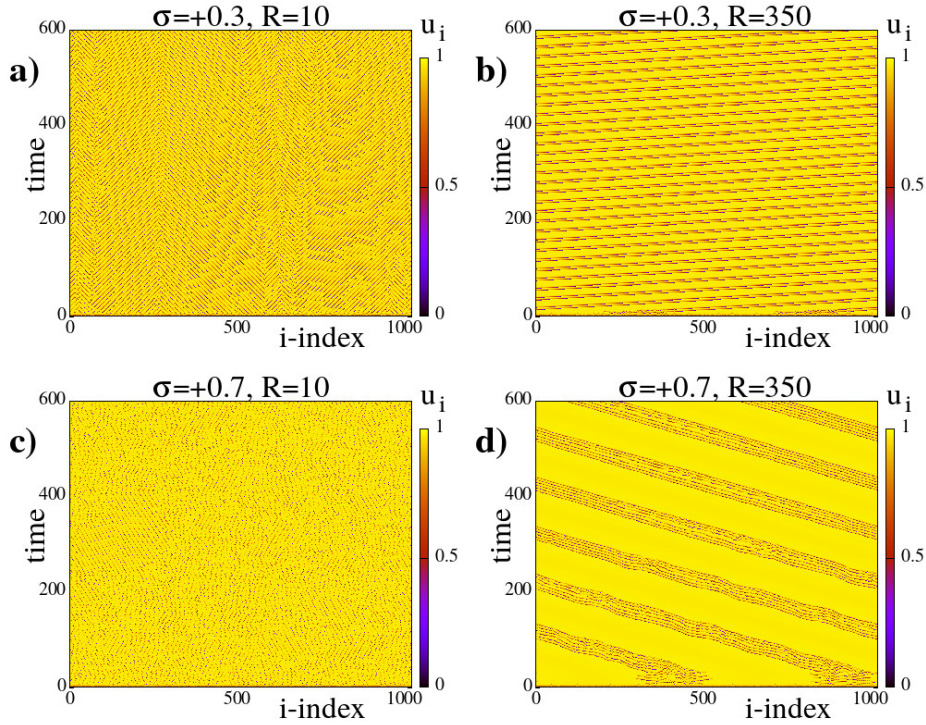


Fig. B.1 Synchronization patterns for inhibitory coupling without link plasticity. Typical spacetime plots for a) $\sigma = 0.3$ and $R = 10$, b) $\sigma = 0.3$ and $R = 350$, c) $\sigma = 0.7$ and $R = 10$, and d) $\sigma = 0.7$ and $R = 350$. All other parameter values are as in Fig. 1 and in appendix A, Fig. A.1. Simulations start from the same random initial conditions in $u_i(t = 0)$.

References

1. M. J. Panaggio and D. Abrams. Chimera states: Coexistence of coherence and incoherence in networks of coupled oscillators. *Nonlinearity*, 28:R67–R87, 2015.
2. E. Schöll. Synchronization patterns and chimera states in complex networks: Interplay of topology and dynamics. *European Physical Journal – Special Topics*, 225:891–919, 2016.
3. O. E. Omel’chenko. The mathematics behind chimera states. *Nonlinearity*, 31:R121, 2018.
4. S. Majhi, B. K. Bera, D. Ghosh, and M. Perc. Chimera states in neuronal networks: A review. *Physics of Life Reviews*, 28:100–121, 2019.
5. A. Zakharova. *Chimera Patterns in Networks: Interplay between Dynamics, Structure, Noise, and Delay*. Understanding Complex Systems, Springer International Publishing, 2020.
6. Y. Kuramoto and D. Battogtokh. Coexistence of coherence and incoherence in nonlocally coupled phase oscillators. *Nonlinear Phenomena in Complex Systems*, 5:380, 2002.
7. D. M. Abrams and S. H. Strogatz. Chimera states for coupled oscillators. *Physical Review Letters*, 93:174102, 2004.
8. W. Gerstner and W. M. Kistler. *Spiking neuron models: Single neurons, populations, plasticity*. Cambridge University Press, Cambridge, 2002.
9. E. R. Kandel, J. H. Schwartz, T. M. Jessell, S. A. Siegelbaum, and A. J. Hudspeth. *Principles of Neural Science, 5th Edition*. The McGraw-Hill Companies, Inc., New York, 2013.
10. W. M. Haddad, Q. Hui, and J. M. Bailey. Human brain networks: Spiking neuron models, multistability, synchronization, thermodynamics, maximum entropy production, and anesthetic cascade mechanisms. *Entropy*, 16:3939–4003, 2014.
11. P. Brodal. *The central nervous system*. Oxford University Press, Oxford, 2016.
12. H. R. Wilson and J. D. Cowan. A mathematical theory of the functional dynamics of cortical and thalamic nervous tissue. *Kybernetik*, 13:55–80, 1973.
13. A. Ewald, L. Marzetti, F. Zappasodi, F. C. Meinecke, and G. Nolte. Estimating true brain connectivity from EEG/MEG data invariant to linear and static transformations in sensor space. *Neuroimage*, 60:476–488, 2012.
14. I. Neuner, J. Arrubla, C. J. Werner, K. Hitz, F. Boers, W. Kawohl, and N.J. Shah. The default mode network and EEG regional spectral power: a simultaneous fMRI-EEG study. *PLoS One*, 9:e88214, 2014.
15. C. Andreou, H. Frielinghaus, J. Rauh, M. Mussmann, S. Vauth, P. Braun, G. Leicht, and C. Mulert. Theta and high-beta networks for feedback processing: a simultaneous EEG-fMRI study in healthy male subjects. *Transl. Psychiatry*, 7:e1016, 2017.
16. M. Butz, F. Wöörötter, and A. van Ooyen. Activity-dependent structural plasticity. *Brain Research Reviews*, 60(2):287–305, 2009.
17. M. Breakspear. Dynamic models of large-scale brain activity. *Nature Neuroscience*, 20:340–352, 2017.
18. I. Omelchenko, O. E. Omel’chenko, P. Hövel, and E. Schöll. When nonlocal coupling between oscillators becomes stronger: patched synchrony or multi-chimera states. *Physical Review Letters*, 110:224101, 2013.
19. I. Omelchenko, A. Provata, J. Hizanidis, E. Schöll, and P. Hövel. Robustness of chimera states for coupled FitzHugh-Nagumo oscillators. *Physical Review E*, 91:022917, 2015.
20. S. Olmi, A. Politi, and A. Torcini. Collective chaos in pulse-coupled neural networks. *Europhysics Letters*, 92:60007, 2010.
21. S. Olmi, E. A. Martens, S. Thutupalli, and A. Torcini. Intermittent chaotic chimeras for coupled rotators. *Physical Review E*, 92:030901, 2015.
22. N. D. Tsigkri-DeSmedt, J. Hizanidis, P. Hövel, and A. Provata. Multi-chimera states and transitions in the leaky integrate-and-fire model with nonlocal and hierarchical connectivity. *European Physical Journal - Special Topics*, 225:1149–1164, 2016.
23. N. D. Tsigkri-DeSmedt, I. Koulterakis, G. Karakos, and A. Provata. Synchronization patterns in lif neuron networks: Merging nonlocal and diagonal connectivity. *The European Physical Journal B*, 91:305, 2018.
24. A. Politi, E. Ullner, and A. Torcini. Collective irregular dynamics in balanced networks of leaky integrate-and-fire neurons. *European Physical Journal: Special Topics*, 227:1185–1204, 2018.
25. S. Olmi, , and A. Torcini. Chimera states in pulse coupled neural networks: the influence of dilution and noise. In F. Corinto and A. Torcini, editors, *Nonlinear Dynamics in Computational Neuroscience*, chapter 5, pages 65–79. PoliTo Springer Series, Cham, Switzerland, 2019.

26. A. Schmidt, T. Kasimatis, J. Hizanidis, A. Provata, and P. Hövel. Chimera patterns in two-dimensional networks of coupled neurons. *Physical Review E*, 95:032224, 2017.
27. G. Argyropoulos, T. Kasimatis, and A. Provata. Chimera patterns and subthreshold oscillations in two-dimensional networks of fractally coupled leaky Integrate-and-Fire neurons. *Physical Review E*, 99:022208, 2019.
28. T. Kasimatis, J. Hizanidis, and A. Provata. Three-dimensional chimera patterns in networks of spiking neuron oscillators. *Physical Review E*, 97:052213, 2018.
29. C. R. Laing and C. C. Chow. Stationary bumps in networks of spiking neurons. *Neural Computations*, 13:1473–1494, 2001.
30. C. R. Laing and O. Omel’chenko. Moving bumps in theta neuron networks. *Chaos*, 30(4):043117, 2020.
31. C. R. Laing. Interpolating between bumps and chimeras. *Chaos*, 31(11):113116, 2021.
32. I. Franović, O. E. Omel’chenko, and M. Wolfrum. Bumps, chimera states, and Turing patterns in systems of coupled active rotators. *Physical Review E*, 104:L052201, 2021.
33. N. D. Tsigkri-DeSmedt, J. Hizanidis, E. Schöll, P. Hövel, and A. Provata. Chimeras in leaky Integrate-and-Fire neural networks: effects of reflecting connectivities. *The European Physical Journal B*, 90:139, 2017.
34. A. Provata, J. Hizanidis, K. Anesiadis, and O. Omel’chenko. Mechanisms for bump state localization in networks of interacting neurons: the case of leaky integrate-and-fire networks in two dimensions. *submitted*, 2014.
35. A. Provata. Chimera states formed via a two-level synchronization mechanism. *Journal of Physics: Complexity*, 1:025006, 2020.
36. A. Provata. Amplitude chimeras and bump states with and without frequency entanglement: a toy model. *Journal of Physics: Complexity*, 5:025011, 2024.
37. I. A. Lazarevich, S. V. Stasenko, and V. B. Kazantsev. Synaptic multistability and network synchronization induced by the neuron–glial interaction in the brain. *JETP Letters*, 105:210–213, 2017.
38. D. O. Hebb. *The organization of behavior: A neuropsychological theory*. John Wiley and Sons, Inc, New York, 1949.
39. D. I. Choi and B.-K. Kaang. Interrogating structural plasticity among synaptic engrams. *Current Opinion in Biology*, 75:102552, 2022.
40. M. Pallares Di Nunzio and F. Montani. Spike timing-dependent plasticity with enhanced long-term depression leads to an increase of statistical complexity. *Entropy*, 24:1384, 2022.
41. R. Berner, T. Gross, C. Kuehn, J. Kurths, and S. Yanchuk. Adaptive dynamical networks. *Physics Reports*, 1031:1–59, 2023.
42. P. Holme and J. Saramäki. Temporal networks. *Physics Reports*, 519:97–125, 2012.
43. L. M. Lapicque. Recherches quantitatives sur l’excitation électrique des nerfs. *J. Physiol. Pathol. Générale*, 9:567–578, 1907.
44. N. Brunel and M. C. W. van Rossum. Lapicque’s 1907 paper: from frogs to integrate-and-fire. *Biological Cybernetics*, 97(5):337–339, 2007.
45. L. F. Abbott. Lapicque’s introduction of the integrate-and-fire model neuron (1907). *Brain Research Bulletin*, 50(5/6):303–304, 1999.
46. S. Luccioli and A. Politi. Irregular collective behavior of heterogeneous neural networks. *Physical Review Letters*, 105:158104, 2010.
47. R. Smidtaite, G. Q. Lu, and M. Ragulskis. Image entropy for the identification of chimera states of spatiotemporal divergence in complex coupled maps of matrices. *Entropy*, 21:523, 2019.
48. N. Caporale and D. Yang. Spike Timing-Dependent Plasticity: A Hebbian learning rule. *Annual Review of Neuroscience*, 31:25–46, 2008.
49. A. Lin, R. Yang, and et al. Network statistics of the whole-brain connectome of *Drosophila*. *Nature*, 634:153–165, 2024.
50. K. L. Scheffer and et. al. A connectome and analysis of the adult *Drosophila* central brain. *eLife*, 9:e57443, 2020.